Physics – Uspekhi **66** (6) 576 – 585 (2023)

REVIEWS OF TOPICAL PROBLEMS PACS numbers: 62.20.D –, **63.20. – e,** 65.40.Ba, 71.20.Be, **72.15. – v,** 75.47.Np

Thermodynamic, elastic, and electronic properties of substances with a chiral crystal structure: MnSi, FeSi, and CoSi

S M Stishov, A E Petrova

DOI: https://doi.org/10.3367/UFNe.2021.11.039104

Contents

Abstract. Transition metal silicides crystallizing in a B20 chiral structure whose space group $P2_13$ does not contain an inversion center feature a number of remarkable properties that have been studied for many decades. We analyze investigations of MnSi, FeSi, and CoSi, the most studied materials of this class, which are a sequence of a magnetic metal, a semiconductor, and a semimetal. Each of these materials exhibits the influence of spatial symmetry on certain features of the electronic and phonon spectra, some of which have been discovered quite recently.

Keywords: transition metals, phonons, elastic constants, electronic properties, magnetic properties

1. Introduction

Transition metal silicides with a noncentrosymmetric B20-type crystalline structure have greatly attracted researchers' attention for decades due to their nontrivial magnetic and electrical properties. Recently, interest in compounds of this kind, which also includes a number of germanates, has significantly increased due to their topological features determined by the specific symmetry of the crystal lattice. The violation of spatial symmetry in the B20 structural type results in the existence of special points, including Weyl points, in the electronic and phonon spectra, characterized by topological Chern numbers.[1] However, semimetals such as CoSi and RhSi, and possibly CoGe and RhGe, are special compounds that exhibit exotic fermionic excitations of various kinds. For all that, in this review, we only describe and analyze the properties of MnSi, FeSi, and CoSi as the most studied materials of this class.

S M Stishov (*), **A E Petrova**
Lebedev Physical Institute, Russian Academy of Sciences,
Leninskii prosp. 53, 119991 Moscow, Russian Federation
E-mail: (*)stishovsm@lebedev.ru

Received 28 October 2021
Uspekhi Fizicheskikh Nauk **193** (6) 614 – 624 (2023)
Translated by M Zh Shmatikov

MnSi, FeSi, and CoSi crystallize in a noncentrosymmetric cubic structure B20, characterized by the space group $P2_13$, which does not contain a center of symmetry. The primitive elementary cell contains four formula units. The B20 structural type includes right and left enantiomorphic forms (Fig. 1). The coordinates of the Me and Si atoms of the right form are (X, X, X), $(1/2 + X, 1/2 - X, -X)$, $(-X, 1/2 + X, 1/2 - X)$, $(1/2 - X, -X, 1/2 + X)$, where $X_{\mathrm{Me}} \cong 0.14$, $X_{\mathrm{Si}} \cong 0.85$. The left form corresponds to the substitution $X \to (1 - X)$ (see Fig. 1).

MnSi is an itinerant magnet with a magnetic phase transition point at a temperature of about 29 K. The $P2_13$ spatial group allows the existence of a nonzero value of the Dzyaloshinskii–Moriya term in energy, which causes the appearance of long-wavelength modulation of the magnetic spin structure in MnSi. Consequently, the magnetic order identified in MnSi is a helical spin structure with a step of 180 Å [3–6]. The magnetic phase transition in MnSi has been actively studied (see, for example, Refs [7–9]). Nevertheless, the nature of some specific features of the phase transition in MnSi is still a matter of discussion. In particular, discussed is the behavior of the thermal expansion coefficient and heat capacity, which exhibit pronounced anomalies at temperatures slightly above the phase transition temperature [7, 8, 10, 11].

FeSi, a highly correlated semiconductor with a small band gap of about 0.05 eV, exhibits metallic properties at temperatures above 100 K [12–17]. Angle-Resolved Photo-Emission Spectroscopy (ARPES) shows that the band gap in FeSi disappears at high temperatures [18–21]. One of the interesting features of FeSi is the increase in its magnetic

[1] Chern numbers, which only take integer values, characterize the topology of certain quantum mechanical systems and arise as a result of integrating the Berry curvature over a closed surface in the momentum space. This is similar to integration of the Gaussian curvature over a closed surface in differential geometry, which leads to integer values of a quantity, called the Euler characteristic and actually related to the number of holes in a particular figure. Thus, like the Euler characteristic, the Chern number, sometimes referred to as the topological charge, is a topological invariant insensitive to deformations of the figure, as long as the number of holes remains unchanged. (See [1, 2] for details.).

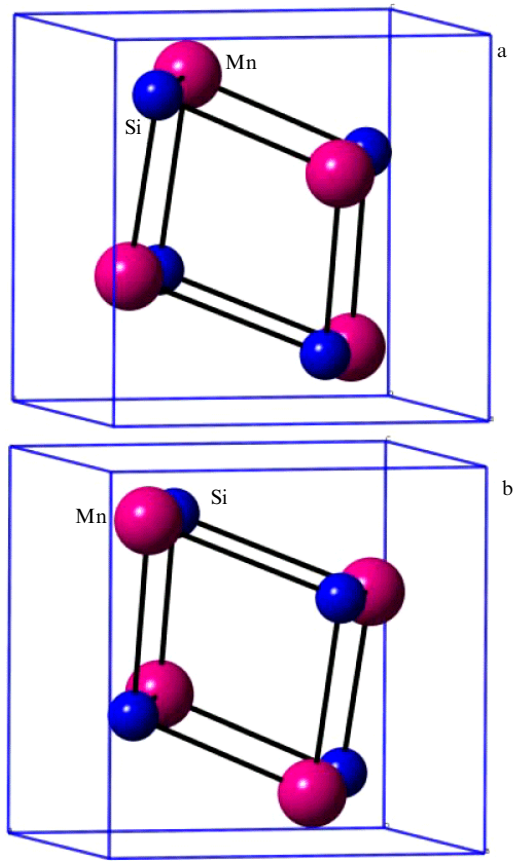

Figure 1. Crystal structure of the right (a) and left (b) forms of B20-type compounds.

susceptibility at temperatures above 100 K, which reaches a broad maximum at 500 K followed by Curie–Weiss-type behavior. The electrical conductivity of FeSi also sharply increases in the same temperature range along with magnetic susceptibility. No magnetic ordering has been found in FeSi [22].

CoSi is a diamagnetic semimetal with a very high residual resistance, which suggests the presence of a fairly large number of defects [23]. CoSi has been extensively studied as a potential material for thermoelectric applications [23–25]. Currently, CoSi, as show below, is being actively explored as a kind of model material demonstrating new types of Fermi quasiparticles.

It should be noted that the electronic properties of MnSi, FeSi, and CoSi generally agree well with calculations of the band structure and density of states (see, for example, [26–29] and subsequent sections of this review). The closing of the gap in FeSi at high temperatures is found in the calculations [30].

We present here experimental and theoretical results that characterize the elastic properties, heat capacity, magnetic susceptibility, and electrical resistance of MnSi, FeSi, and CoSi single crystals. A significant part of the data presented in this review is based on our studies [7, 8, 31–41]. We point out that MnSi, FeSi, and CoSi compounds melt congruently and, consequently, their single crystals can be obtained directly from the melt. The MnSi and CoSi single crystals studied in our work were grown by the Bridgman method, while the FeSi single crystal was obtained by the Czochralski method. However, perfect small-size single crystals of B20 compounds, suitable for photoemission spectroscopy, can also be obtained by the methods of solution in a melt and chemical transport. Table 1, taken from [33], displays the crystal lattice parameters and their chemical composition. As can be seen, the lattice parameters of MnSi, FeSi, and CoSi change very little in accordance with the values of the metallic radii for Mn, Fe, and Co [47]. This observation indicates that the total energies of these substances are not sensitive to the details of their electronic and magnetic structures. Electron probe microanalysis shows some deviations from the stoichiometric chemical composition of compounds, which is common for silicides (see also [48]). We note that deviations from stoichiometry increase with an increase in the number of valence states in the CoSi–FeSi–MnSi series.

Table 1. Lattice parameters a and chemical composition of MnSi, FeSi, and CoSi.

	a, Å	Atomic %	
		Metal	Si
MnSi	4.5598(2) [33] 4.558(2) [42] 4.5559(3) [43]	50.63	49.37
FeSi	4.4827(1) [33] 4.485(1) [44] 4.48798(9) [45]	50.16	49.84
CoSi	4.444(1) [33] 4.4438(6) [33] 4.438 [46]	50.07	49.93

2. Heat capacity and phonon spectra

Figures 2 and 3 show the measured values of the heat capacity of MnSi, FeSi, and CoSi based on data from [31–33, 35]. The measurements were carried out both by the classical method using an adiabatic calorimeter and by the relaxation method included in the Physical Properties Measurement System (PPMS, Quantum Design). Both yielded quite consistent results. As can be seen from Fig. 2, the heat capacity of MnSi, a magnetic material, differs significantly from that of nonmagnetic FeSi and CoSi over the entire temperature range, including the paramagnetic region of MnSi. Apparently, this situation indicates the existence of significant spin fluctuations in the paramagnetic phase of MnSi. It is of interest that the theoretical value of the lattice heat capacity of MnSi (see Fig. 2 and below) is in good agreement with the experimental data for nonmagnetic FeSi and CoSi, thus allowing us to estimate the magnitude of the magnetic contribution to the heat capacity of MnSi.

The heat capacity divided by temperature, C_p/T, for MnSi, FeSi, and CoSi is shown in Fig. 3. A noticeable C_p/T anomaly with a sharp peak is indicative of a magnetic phase transition in MnSi. An extrapolation of the C_p/T value for MnSi to zero temperature yields an extremely large value of the Sommerfeld constant: $\gamma = 36$ mJ mol^{-1} K^{-2}, which determines the electron contribution to the heat capacity [32]. The heat capacity C_p for FeSi is described in [15] in the temperature range of 0.2–10 K as a combination of conventional low-temperature electronic and lattice contributions and two Schottky anomalies. Surprisingly, the value $\gamma =$ 1.1 mJ mol^{-1} K^{-2} obtained in [15] is close to the values typical of simple metals. However, based on the data presented in Fig. 3, we cannot confirm the conclusion about the finite C_p/T value at $T \to 0$ for FeSi. On the other hand,

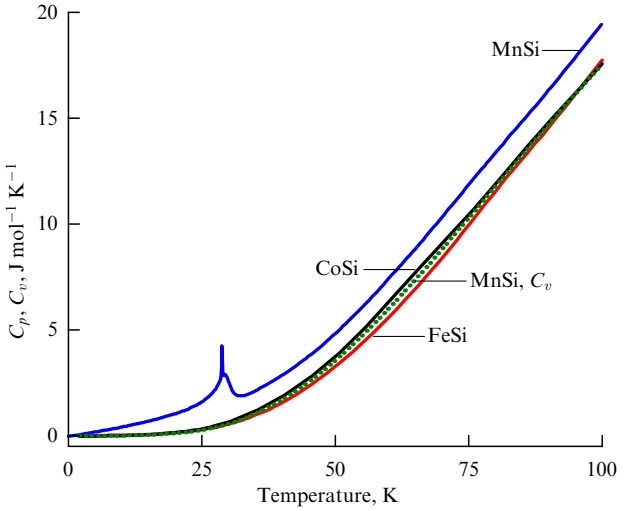

Figure 2. Experimental temperature dependence of the heat capacity of MnSi, FeSi, and CoSi. For comparison, the calculated temperature dependence of the phonon heat capacity of MnSi is presented, which makes it possible to estimate the magnitude of the magnetic contribution. (According to [31–33, 35, 50].)

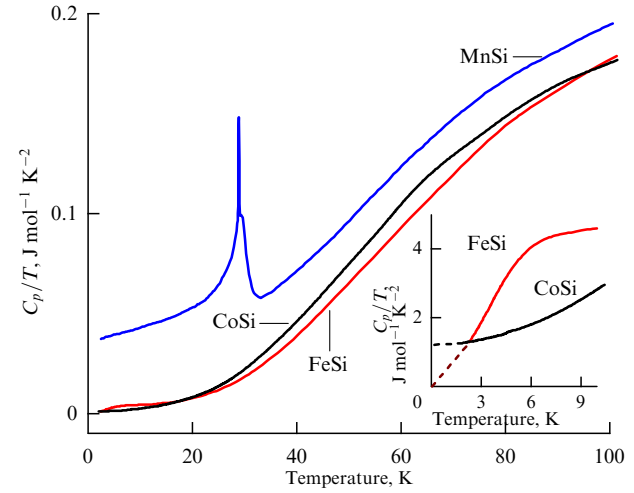

Figure 3. Temperature dependence of the C_p/T ratio for MnSi, FeSi, and CoSi. Inset shows the behavior of C_p/T for FeSi, CoSi at $T < 10$ K [31–33, 35].

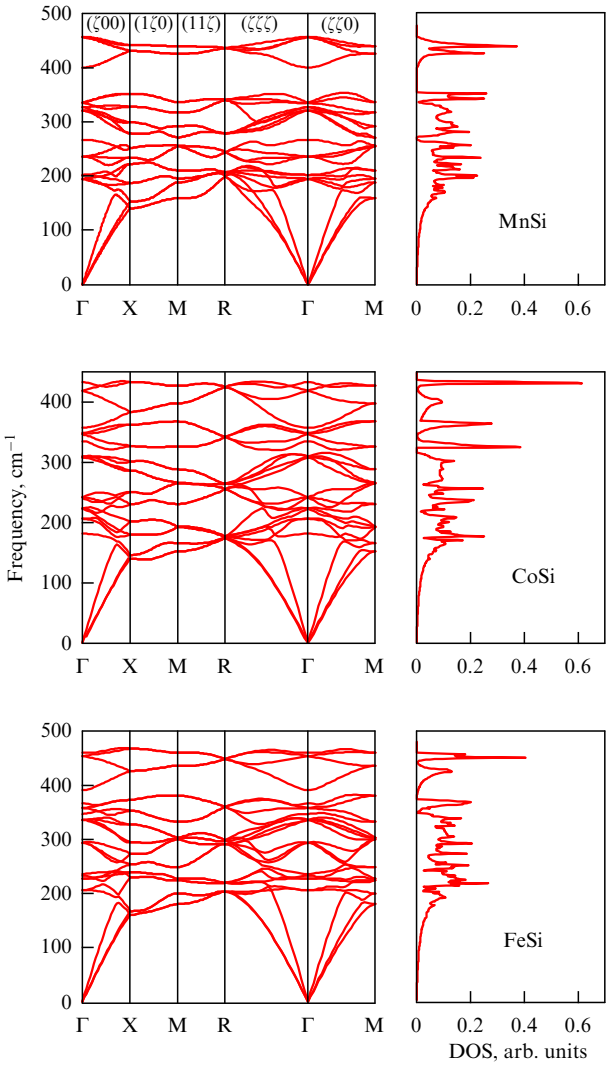

Figure 4. Phonon spectra and density of phonon states for MnSi, FeSi, and CoSi according to calculations made in [50] (see text). All calculations were performed as part of a collaboration with the late Evaz Isaev (Linkoping University, Sweden) and for the most part have not been published before.

the heat capacity of CoSi undoubtedly contains a linear temperature term γT with $\gamma = 1.2$ mJ mol^{-1} K^{-2} (see Fig. 3).

Concurrently with the measurements, phonon spectra and lattice heat capacity were calculated. The computation technique is briefly described below (for more details, see [35]). Static calculations of the total energy were performed in the spin polarized version of the density functional theory to obtain a completely relaxed structure, including the equilibrium lattice parameter and positions of the Me and Si atoms. The phonon dispersion relations in MnSi were calculated using the linear response method implemented in the Quantum ESPRESSO software package. Electron-ion interactions were described using supersoft pseudopotentials, while exchange-correlation effects were considered in the generalized-gradient approximation. The dispersion relations for phonons were calculated using the matrix of force constants in real space obtained using the fast Fourier transform of dynamic matrices. The phonon density of states (Phonon Density Of States, PhDOS) and thermodynamic properties of silicides were calculated using the QHA program (E Isaev, QHA project). In some cases, the results of calculations of the density of phonon states were verified by direct measurements of the PhDOS using neutron scattering on polycrystalline materials [35]. We should also point out the experimental work devoted to the inelastic scattering of neutrons by an MnSi single crystal and subsequent calculations aimed at reconstructing the phonon spectrum of MnSi [36, 37]. The effect of broken spatial symmetry on short-wavelength acoustic phonons in MnSi was studied in [49] using inelastic X-ray scattering. It was found that the twofold degeneracy of transverse acoustic modes is removed due to chiral symmetry.

The phonon contributions to the heat capacity can be easily calculated using the obtained PhDOS (Fig. 4). In fact, the calculations provide the values C_v (Fig. 5) (see also Fig. 2), which are used to analyze the experimental data on C_p. However, estimates show that the value $C_p - C_v$ does not exceed 0.1 J mol^{-1} K^{-2} in the studied temperature range. This difference is too small to affect our conclusions. We note that the theoretical phonon heat capacity of MnSi presented in

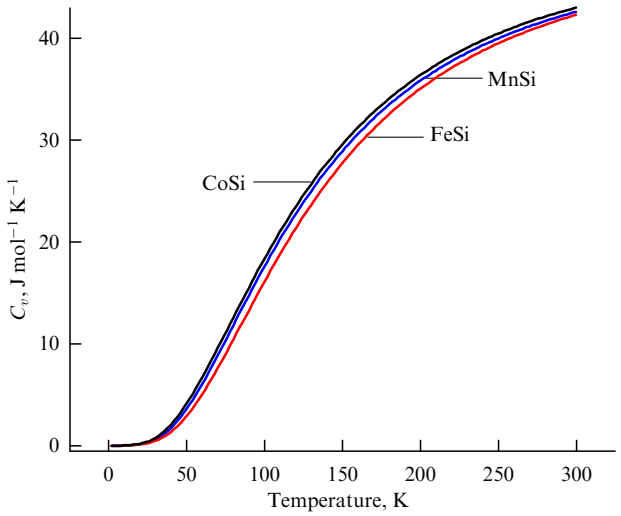

Figure 5. Phonon heat capacity of MnSi, FeSi, and CoSi according to calculations made in [50] (see text).

Table 2. Elastic moduli of MnSi, FeSi, and CoSi, 10^{12} dyn cm^{-2} (a is the lattice parameter).

MnSi	$a = 4.5598$ Å		
c_{ij}	$T = 6.5$ K [33]	$T = 0$ [51]	$T = 0$ [35, 50]
c_{11} c_{44} c_{12}	3.2057 1.2615 0.8523	3.01209 1.30054 0.54	3.4 1.08 1.03
FeSi	$a = 4.483$ Å		
c_{ij}	$T = 6.5$ K [33]	$T = 50$ K [60]	$T = 0$ [35, 50]
c_{11} c_{44} c_{12}	3.4626 1.3916 1.0576	3.37 1.35 0.77	3.82 1.37 1.4
CoSi	$a = 4.444$ Å		
c_{ij}	$T = 6.5$ K [33]	$T = 0$ [51]	$T = 0$ [35, 50]
c_{11} c_{44} c_{12}	3.5432 1.1847 1.3323	3.35016 1.23184 0.95	3.52 1.10 1.16

Table 3. Debye temperature* Θ_D, K.

MnSi			
$\Theta_D(c_{ij})$ [33]	$\Theta_D(c_{ij})$ [51]	$\Theta_D(C_p)$ [52]	$\Theta_D(C_v)$ [35, 50]
660	606	515	709.77
FeSi			
$\Theta_D(c_{ij})$ [33]	$\Theta_D(C_p)$ [53]	$\Theta_D(V(T))$ [54]	$\Theta_D(C_v)$ [35, 50]
680	457	445	741.43
CoSi			
$\Theta_D(c_{ij})$ [33]	$\Theta_D(c_{ij})$ [51]	$\Theta_D(C_v)$ [55]	$\Theta_D(C_v)$ [35, 50]
625	506	487 ± 6	629.93

* Presented in parentheses are the methods used for estimating Θ_D: c_{ij} — calculations based on experimental values of elastic moduli, C_p — calculations based on experimental values of heat capacity, C_v — estimate based on theoretical calculations of heat capacity at constant volume, $V(T)$ — calculation based on experimental values of thermal volume expansion.

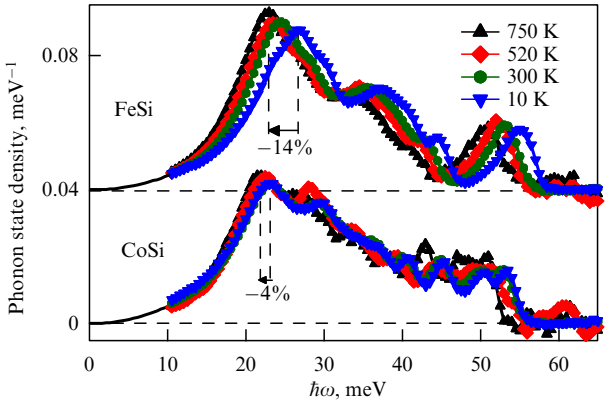

Figure 6. Normalized density of phonon states for FeSi and CoSi at various temperatures according to data from [30].

Figs 2 and 5 is consistent with the results of independent calculations that follow from [36, 37]. The calculated lattice parameters and the values of sound velocities and elastic constants turned out to be in good agreement with the experimental data (Table 2). The calculated low-temperature values of the effective Debye temperature agree very well with the experimental values obtained from the elastic properties (Table 3).

The results of calculations of heat capacity are shown in Fig. 5 (see also Fig. 2). As can be seen from the presented data, the experimental and calculated results are in good agreement with each other, with the exception of the results for MnSi. In this connection, study [30] should be noted, where the temperature dependence of the density of phonon states for FeSi and CoSi was examined. As can be seen from Fig. 6, the temperature dependences of the phonon spectra for FeSi and CoSi are fairly dissimilar. In the case of CoSi, a relatively small shift in the density of states of phonons is observed in the temperature range between 10 and 750 K, which is compatible with thermal expansion in this range. On the other hand, the phonon density of FeSi states is significantly softened, with all parts of the spectrum shifted towards lower energies. In particular, the acoustic peak at an energy of about 25 meV in DOS FeSi sharply softens with a decrease in energy by 14% in the temperature range of 10 to 750 K, which is especially noticeable in the range between 10 and 300 K. Apparently, the observed softening of the phonon spectrum is associated with metallization of the substance, which occurs at temperatures much higher than 100 K, and, consequently, it could not be reflected in the results of heat capacity measurements (see Fig. 2). The influence of magnetic moments arising at high temperatures in FeSi on phonon spectra was analyzed in [56].

The topological state of phonons requires some comments. As shown below, the topological states of electronic systems have recently attracted considerable interest. However, topological states can also arise during high-frequency vibrations of the crystal lattice (in a system of phonons), which can significantly affect such important features as thermal conductivity and electron-phonon interaction. The authors of [57] predicted the existence of topological phonons in transition metal monosilicides with a noncentrosymmetric B20 crystal structure, which are, in particular, the subject of this review. As expected, the specificity of topological phonons can be established by direct measurements using

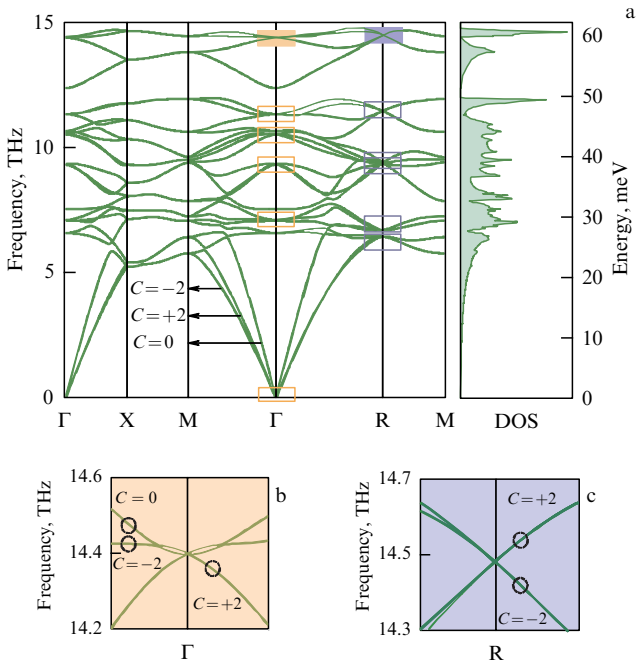

Figure 7. (a) Phonon dispersion in FeSi along highly symmetric directions. Acoustic branches have a Chern number of 0; 2. Orange rectangles enclose Weyl points with spin 1 in the direction Γ, while purple rectangles enclose Dirac points with charge (Chern number) 2 in the direction R. (b) Point Γ is the Weyl point with spin 1. (c) Point R is a Dirac point with charge (Chern number) 2. The '+' and '−' signs identify topological points as sources and sinks.

neutron and X-ray scattering, which was actually done. Figure 7 shows the phonon spectrum and density of FeSi states (see also Fig. 4) with the topological points identified according to calculations in [57]. Subsequent studies of phonon dispersion in FeSi by means of inelastic X-ray scattering led to the experimental discovery of double Weyl points [58].

3. Elastic properties

In this section, we consider the results of studying the elastic properties of MnSi, FeSi, and CoSi. They were determined by measuring the speed of sound using digital echo-pulse technology, based on data from [33, 34, 39, 59]. The results of measurements and calculations are displayed in Figs 8–15 and in Table 2. Low-resolution ultrasonic data for a number of transition metal silicides were published in [51]. The temperature dependence of the elastic moduli of FeSi, measured earlier by resonant ultrasonic spectroscopy [60], generally agrees with our results where they overlap, at temperatures $T > 77$ K, some differences being apparently associated with temperature calibration.

We now proceed to the analysis of data on the elastic properties of MnSi, FeSi, and CoSi. As can be seen from Figs 8 and 9, the values of the elastic constants c_{11} and c_{12} in the MnSi–FeSi–CoSi series change depending on the position of the metal in the periodic table or, in other words, on the number of 3d-valence electrons in these compounds. A small difference in this characteristic of the materials apparently leads to an insignificant change in the binding energies and lattice parameters, although it causes a fairly noticeable difference in the elastic constants. It should be emphasized that this regularity persists despite the specific properties of

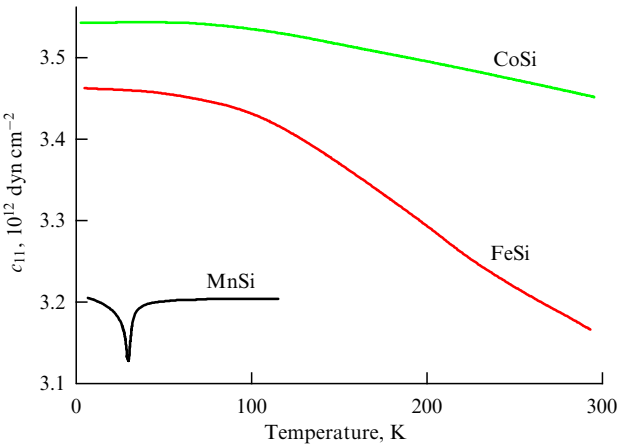

Figure 8. Elastic constants c_{11} of MnSi, FeSi, and CoSi as functions of temperature [33].

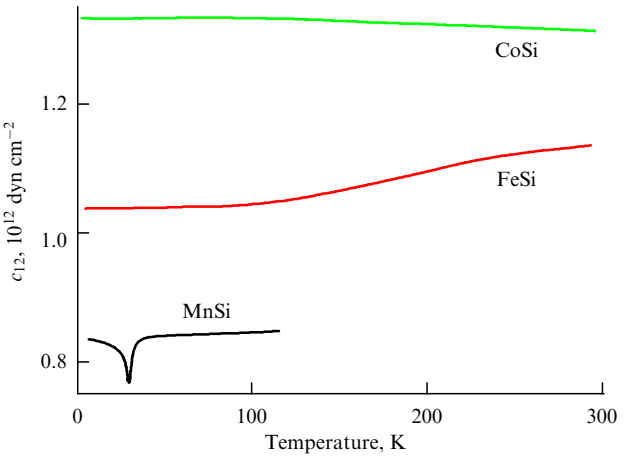

Figure 9. Elastic constants c_{12} of MnSi, FeSi, and CoSi as functions of temperature [33].

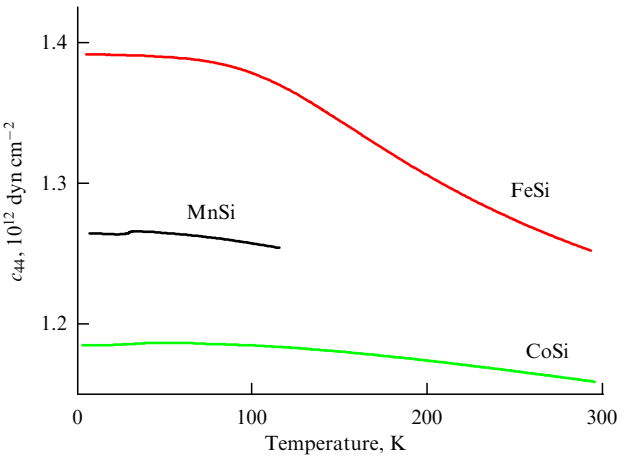

Figure 10. Elastic constants c_{44} of MnSi, FeSi, and CoSi as functions of temperature [33].

the electronic and magnetic structures of the compounds. It is instructive to analyze the situation at low temperatures. Indeed, CoSi, a semimetal with a good metallic value of the Sommerfeld constant, features the largest elastic constants c_{11} and c_{12} followed by the corresponding values for FeSi, a narrow gap semiconductor, and for MnSi, an almost heavy fermionic metal with a helical magnetic structure (see Figs 8

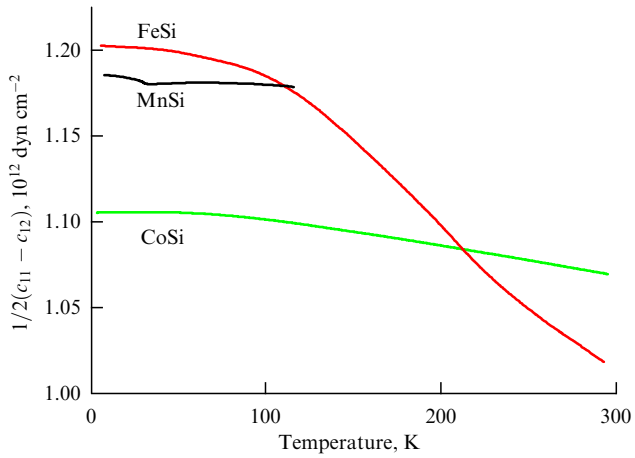

Figure 11. Elastic shear moduli $(c_{11}-c_{12})/2$ of MnSi, FeSi, and CoSi as functions of temperature [33].

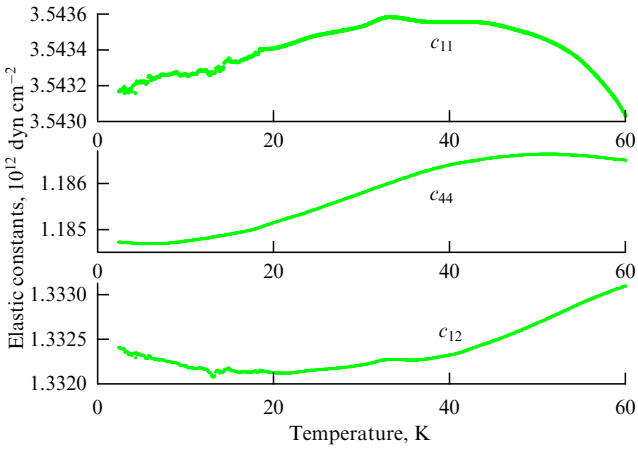

Figure 12. Elastic constants of CoSi as a function of temperature in a detailed representation [33].

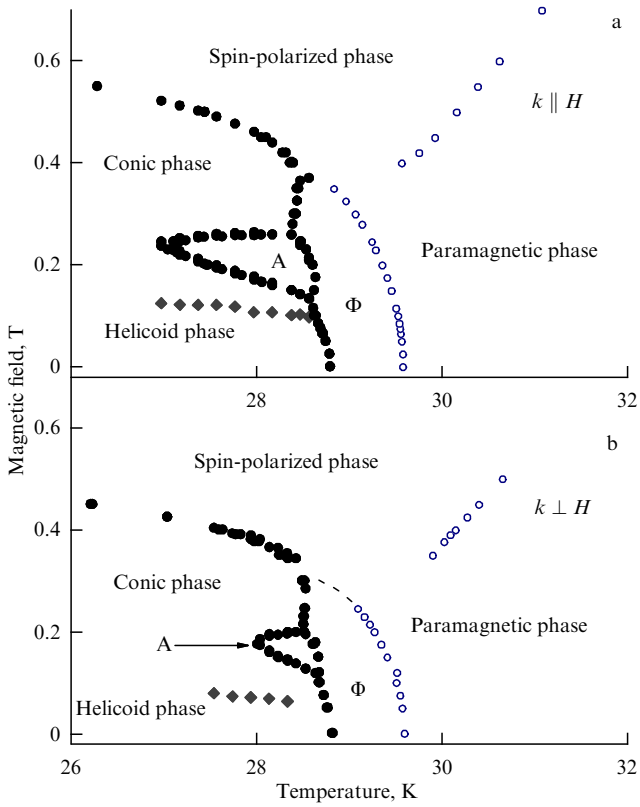

Figure 13. Magnetic phase diagram of MnSi according to [39]. Dark circles are jumps in c_{11} and c_{33} and sound absorption maxima. Circles are the minima in c_{11} and c_{33}. Diamonds are a helicoid-conical transition, Φ is a strongly fluctuating region, and A is a skyrmion crystal. Magnetic field is directed perpendicular (a) or parallel (b) to the (100) plane. As a result, demagnetizing factors for both setups turn out to be completely different, with a smaller value in the perpendicular setup, where the magnetic field is perpendicular to the ultrasonic wave propagation vector, which explains the difference between the scales of panels a and b. It can be seen that a large demagnetizing factor contributes to an increase in the region where a skyrmion crystal exists.

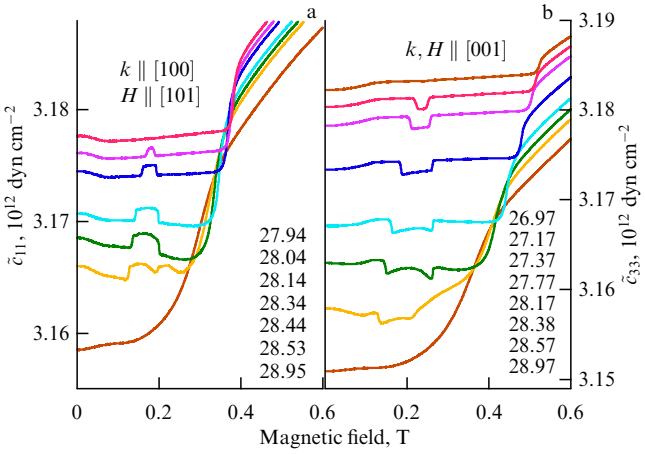

Figure 14. Dependence of longitudinal moduli of elasticity on the magnetic field at various temperatures. Temperature values for each isotherm (from top to bottom) are shown in the lower right corner in panels a and b [39].

and 9). A different situation is observed in the case of shear elastic constants c_{44} (see Fig. 10) and $(c_{11}-c_{12})/2$ (see Fig. 11), which are the largest for FeSi and the smallest for CoSi. It also seems quite natural that CoSi with the highest electron density features the largest bulk modulus $K=(c_{11}+2c_{12})/3$.

However, it is not entirely clear why CoSi should have the smallest shear moduli c_{44} and $(c_{11}-c_{12})/2$ (see Figs 10 and 11). The temperature variations in the elastic properties of the three compounds under consideration are far from trivial. In the case of CoSi, there are no significant features that could be seen at scale (see Figs 8–11); however, examination of the temperature dependence of the elastic constants of CoSi at $T<60$ K with a higher resolution (see Fig. 12) reveals an unusual softening of the elastic constants. The elastic constants c_{11} and c_{44} of FeSi strongly decrease at high temperature compared to those for CoSi, while c_{12} increases anomalously over the entire temperature range. As a result, the shear modulus $(c_{11}-c_{12})/2$ of FeSi sharply decreases at $T>100$ K (see Fig. 11). This behavior is consistent with the closing of the energy gap, as indicated in [18–20]. The elastic constants of MnSi, which control the propagation of longitudinal waves, reveal a significant softening at $T=30$ K and small jumps at $T=28.8$ K, which corresponds to a magnetic phase transition in MnSi. On the contrary, shear elastic moduli do not exhibit any softening and only respond to small bulk deformations [32].

Returning to CoSi, we recall that the temperature derivatives of physical quantities tend to zero at $T\to 0$. As

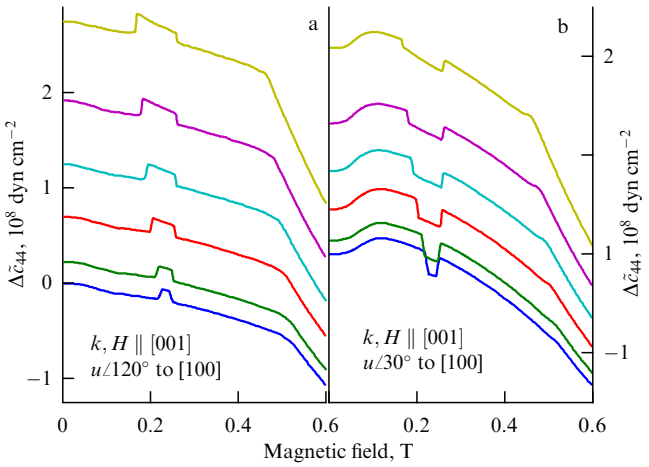

Figure 15. Shear modulus c_{44} measured in the (001) plane with polarization u at an angle of (a) 120° and (b) 30° to the [100] direction. Isotherm temperatures in kelvins from top to bottom are 28.06; 27.84; 27.64; 27.44; 27.24; and 27.14 [39].

can be seen from Figs 8–11, this presumably occurs at $T/\Theta_D \approx 1/6$.

However, the observed tendency of the temperature derivatives to zero does not always occur in a smooth and monotonic way, which is indicated by the temperature dependence of the elastic constants of CoSi displayed in Fig. 12. It can be seen that, with decreasing temperature, the elastic constants of CoSi unexpectedly pass through maxima in the temperature range between 40 and 70 K and continue to change with temperature decreasing to 2.5 K. At the same time, the magnetic susceptibility of CoSi increases at a temperature below 50 K, which is possibly associated with the formation of local magnetic moments [33, 38].

To conclude this section, it is worth dwelling on the results of studying the magnetic phase diagram of MnSi and its skyrmion phase using ultrasonic technology [39] (see also [61, 62]). Skyrmions are topologically protected vortex spin structures of nanometer size, which are formed upon the application of relatively weak magnetic fields in magnetic substances with a noncentrosymmetric crystal lattice. It is the topological properties of skyrmions that inspire optimism regarding their potential application in spintronics. Skyrmions can crystallize forming a kind of vortex lattice. In particular, the 2D crystal lattice of skyrmions observed in MnSi is a hexagonal packing of skyrmion tubes [63, 64]. Figure 13 shows the magnetic phase diagram of MnSi, measured at two orientations of the magnetic field with respect to the direction of propagation of ultrasonic waves, for a plate-shaped sample. The region where the skyrmion phase exists turns out to be very sensitive to the magnitude of the demagnetizing factor and the related homogeneity of the magnetic field in the sample, which, apparently, opens up a way to control skyrmions. On the other hand, it would seem that, in a sample in the form of a sphere or an ellipse with a uniform magnetic field, skyrmions will not exist. However, the results of study [65] show that this hypothesis is not confirmed.

Figures 14 and 15 show the dependences of the elastic constants of an MnSi crystal on the magnetic field at various temperatures. The tilde in the designation of elastic constants indicates that the magnetic field directed perpendicular to the hexagonal axis of the skyrmion crystal, as is the case in the described measurements, breaks the initial symmetry. Consequently, this is the case of a crystal with weak asymmetry in the plane normal to the pseudohexagonal axis. The depressions and bumps in Figs 14 and 15 correspond to abrupt changes in the elastic constants at the boundaries of the skyrmion crystal and the conical phase (see Fig. 13), which is indicative of a first-order phase transition at the interfaces. As a result, we can conclude that a skyrmion crystal features all the characteristics of a true crystal, i.e., finite values of elastic moduli, including shear moduli. This factor is decisive in classifying the substance as a crystal.

4. Electrical and magnetic properties of MnSi, FeSi, and CoSi

The electronic structure of the substances under consideration has been the subject of numerous studies in the past (see, for example, [26–29]). At present, interest in this topic has rekindled in connection with studies of topological points in chiral crystalline structures, to which the structures of these substances can be attributed.

Figure 16 shows the results of band structure calculations for MnSi, FeSi, and CoSi performed in [66] (see also [67]). Band structure calculations were carried out using the density functional theory in the generalized gradient approximation. The spin-orbit interaction was taken into account in all calculations. The calculation results predict a ferromagnetic ground state for MnSi and a nonmagnetic ground state for FeSi and CoSi. However, calculations enable attributing FeSi and CoSi to the class of semiconductors and semimetals, respectively, which agrees with the experimental data. As can be seen from Fig. 16, the Fermi level is located within the band gap in the case of FeSi, while, in the case of CoSi, the Fermi level is slightly below the fourfold band intersection at point Γ near the minimum of the density of states.

Next, we proceed to an analysis of experimental data. The temperature dependence of the resistivities of MnSi, FeSi, and CoSi is shown in Fig. 17. As can be seen, the resistance curve of MnSi exhibits the presence of a magnetic phase transition at $T \approx 29$ K and a trend to saturate at high temperatures. The residual resistance is about 2 μΩ cm, which results in a residual resistivity ratio (RRR) of ≈ 100. Resistivity of FeSi exhibits a nontrivial behavior that includes three different regimes.

Figure 18a shows that, at temperatures below ≈ 100 K, the resistivity can be approximated by an expression for hopping conductivity with a variable hop length. In a narrow temperature range of 100–150 K, the resistance can be described by a standard activation formula with a band gap of $E_g \approx 0.06$ eV, or 690 K (Fig. 18b). At temperatures close to room temperature, the resistance is saturated, which seems premature for a semiconductor with this gap. This probably implies gap closure and transition of FeSi to a metallic state in accordance with results in [18, 19] (see also [12–16]). The electrical resistance of CoSi exhibits a high residual value and a trend to saturate at high temperatures ($\rho_0 \approx 30$ μΩ cm and RRR ≈ 4.5) (see Fig. 17).

The temperature dependence of the magnetic susceptibility of MnSi, FeSi, and CoSi compounds is shown in Fig. 19. The susceptibility curve of MnSi is characterized by a sharp peak at the magnetic phase transition and Curie–Weiss-type behavior at $T > T_c$ (see Refs [31, 32]). The magnetic susceptibility of FeSi passes through a minimum at $T < 80$ K, which indicates the presence of local magnetic

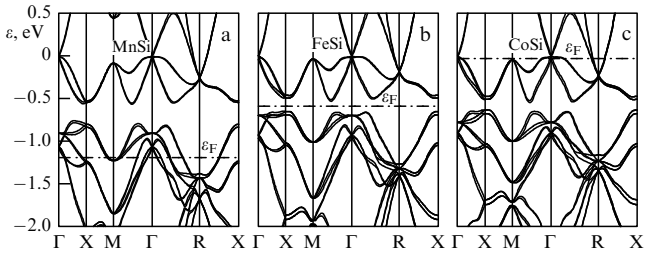

Figure 16. Band structure of (a) MnSi, (b) FeSi, and (c) CoSi with a B20 ($P2_13$) crystal structure. Energy is measured relative to the fourfold intersection of the bands at point Γ. Dashed-dotted line shows position of the Fermi level [66].

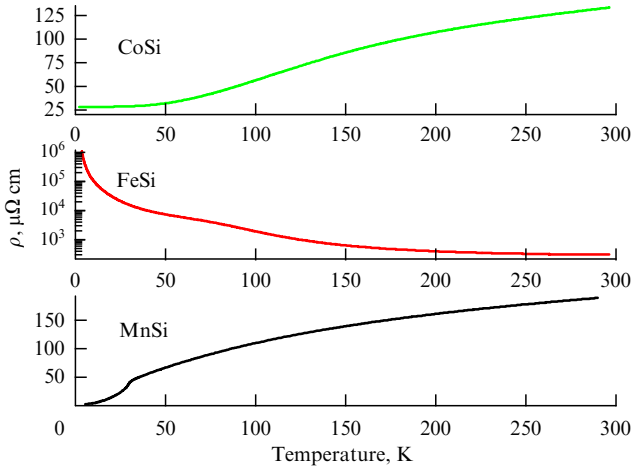

Figure 17. Temperature dependence of the resistivities of MnSi, FeSi, and CoSi [33].

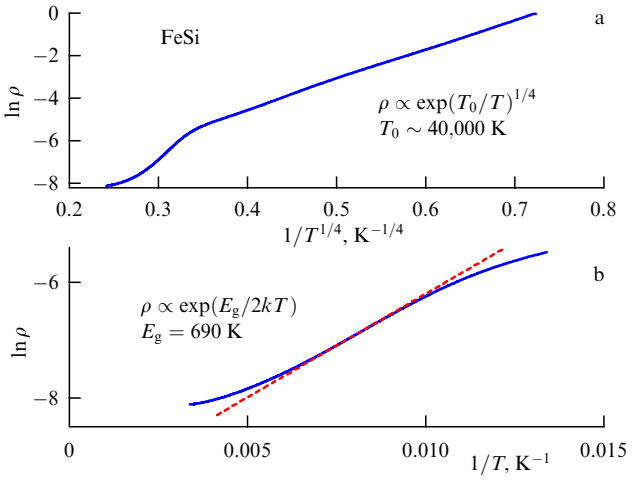

Figure 18. Electrical resistivity of FeSi on a logarithmic scale as a function of $T^{-1/4}$ (a) and T^{-1} (b) [33].

moments induced by impurities or defects at low temperatures. An increase in the susceptibility of FeSi at high temperatures is apparently associated with metallization [12–15]. CoSi is diamagnetic in a wide temperature range, but exhibits paramagnetic behavior at $T < 50$ K. In this connection, it should be noted that silicides always slightly deviate from stoichiometry (see, for example, Table 1) and, therefore, contain structural defects performing as traps for

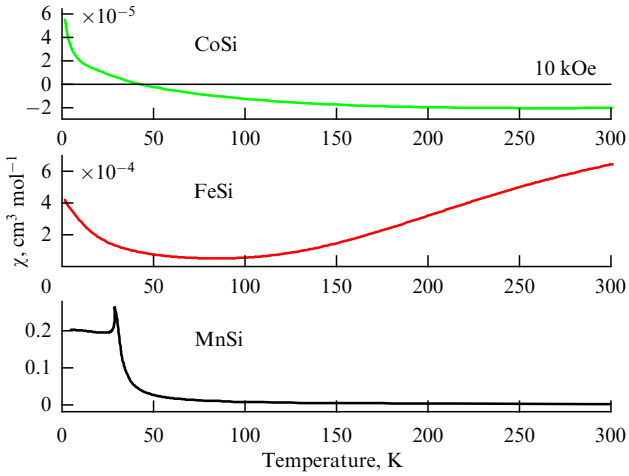

Figure 19. Magnetic susceptibility of MnSi, FeSi, and CoSi as a function of temperature [33].

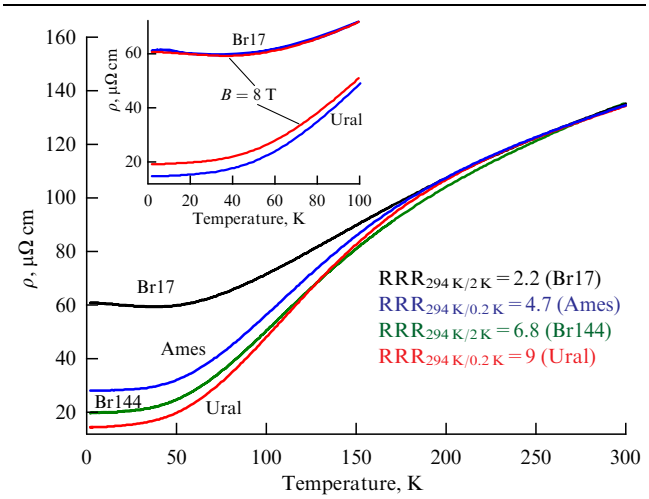

Figure 20. Resistivity of CoSi single crystals as a function of temperature. Inset shows the influence of the magnetic field on resistivity. Note that the magnetoresistance of the Br17 sample is negative, a feature that is virtually unnoticeable in the figure [38].

current carriers at low temperatures with corresponding consequences for magnetic susceptibility.

In view of the special position of CoSi as a diamagnetic semimetal, a number of single crystals of this substance were studied in [38]. Experimental results are presented in Figs 20–22. The resistivity of the samples is shown in Fig. 20. All CoSi samples exhibit a fairly similar behavior of resistivity and magnetic susceptibility. Three samples (Ames, Ural, and Br144) show the presence of a term T^2 in the resistance at temperatures below ≈ 30 K (see Fig. 21). The high but significantly different residual resistances of the samples indicate differences in the concentrations of defects. Due to the high residual resistance along with low RRR and the tendency to saturate at high temperatures, these samples can be classified as so-called highly disordered metals, the resistivity of which can be described using the parallel resistor model [68, 69]. This model, although not fully explained theoretically, reflects the situation when the mean free path, limited by defects, becomes comparable to the interatomic distance [70]. It should be noted that the high temperature asymptotic values of the resistivity of various CoSi samples are almost the same and do not depend on the

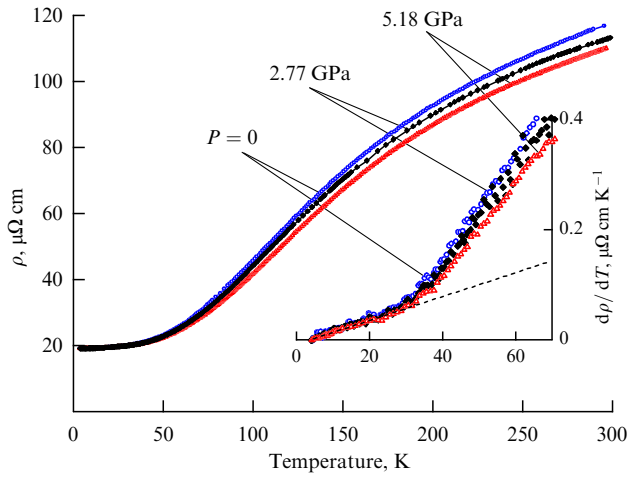

Figure 21. Temperature dependence of electrical resistance ρ and its temperature derivative $d\rho/dT$ (in the inset) of a CoSi Ames single crystal at various pressures. Dashed line in the inset is an extrapolation of the linear part of $d\rho/dT$ [38].

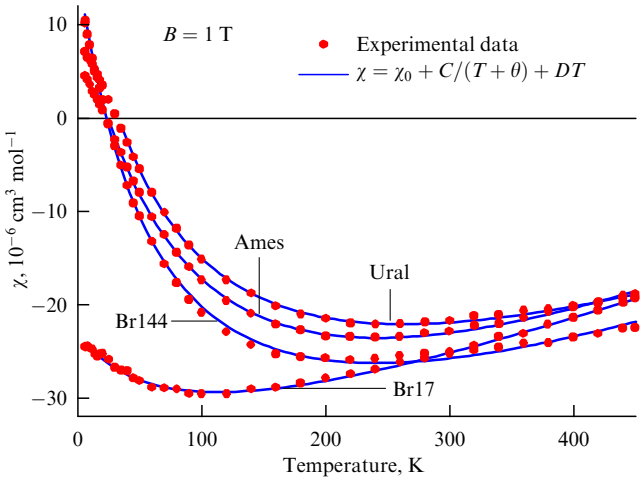

Figure 22. Magnetic susceptibility of CoSi single-crystal samples [38].

residual resistance, which is consistent with the parallel resistor model. This behavior is an obvious example of violation of the Matthiessen rule, which is another feature inherent in highly disordered metals [71]. In the extreme case of a high defect concentration, the temperature coefficient of resistivity $d\rho/dT$ can become negative [68, 71], which is exactly the case observed in the Br17 sample (see Fig. 20). To check the nonmagnetic nature of the observed characteristics of CoSi, the resistivity of all samples was measured in a strong magnetic field (8 T) (see some examples in Fig. 20). As seen in the inset to Fig. 20, a field of 8 T does not destroy the minimum of the resistivity of the Br17 sample. It should be noted that the relative change in magnetoresistance ($\Delta\rho/\rho$, where $\Delta\rho$ is the change in resistivity in a magnetic field) is normal (positive) for the Ural, Ames, and Br144 samples, while for the Br17 sample it sometimes has a small negative value.

We now proceed to Fig. 22, which shows the magnetic susceptibility of four CoSi samples. It should be noted that the CoSi sample shown in Figs 17 and 19 is also presented in Figs 20–22 under the name Ames.

As can be seen, the magnetic susceptibility of the CoSi samples, being diamagnetic at high temperatures, tends to zero with decreasing temperature and even crosses the zero

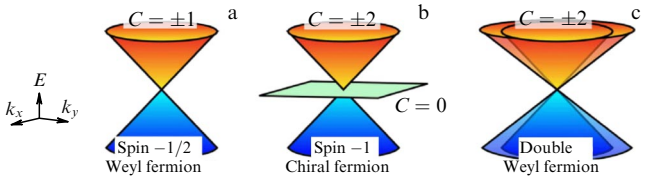

Figure 23. Schematic representation of dispersion in a 3D $E-k$ space for a Weyl fermion with spin $-1/2$ (a), a chiral fermion with spin -1 (b), and a double Weyl fermion (c) [77].

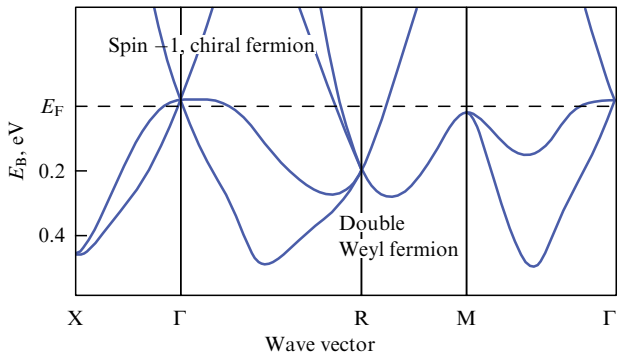

Figure 24. Band structure of CoSi near E_F along high-symmetry directions of the Brillouin zone calculated in Ref. [77] without taking into account spin-orbit interaction (see Fig. 16 in this connection).

line in the case of the Ames, Ural, and Br144 samples, becoming paramagnetic at $T < 25$ K. A sharp increase in the paramagnetic magnetic susceptibility at low temperatures reveals the existence of paramagnetic moments. All magnetic susceptibility curves in Fig. 22 can be successfully approximated by the formula $\chi = \chi_0 + DT + C/(T + \theta)$, where the first two terms presumably describe the diamagnetic contribution to the susceptibility, while the third term is the standard Curie–Weiss expression describing the magnetic susceptibility of a system of interacting magnetic moments.

Finally, we should briefly turn again to CoSi, whose electronic spectrum demonstrates new topological points and chiral fermions [72–80]. Semimetals containing massless Dirac or Weyl fermions have attracted great attention due to their properties such as low carrier density, high mobility, large negative magnetoresistance, and an unusual photovoltaic effect. In addition to the well-known Weyl fermion with spin $-1/2$, new types of fermion excitations have been discovered, including a chiral fermion with spin -1 and a double Weyl fermion. Recent experiments using ARPES have found that CoSi and its family contain these new types of fermion excitations [74, 75, 77]. Figure 23 shows new types of fermions with Chern numbers that are large compared to the Weyl fermion. Figure 24 shows the localization of new fermions in the first Brillouin zone of CoSi.

We should also point out the discovery of quantum oscillations of the thermoelectric signal [75], the Shubnikov–de Haas [78] effect, and the de Haas–van Alphen [79] effect in CoSi. However, the phenomenon of negative magnetoresistance, which is expected for the case of a topological semimetal, has not yet been reliably observed in CoSi. Nevertheless, attention should be paid to study [81], which reports the detection of negative magnetoresistance in CoSi nanowires.

Further discussion of the topological properties of CoSi is beyond the scope of this review and apparently requires a

separate publication. Nevertheless, we note that CoSi is the only material from the considered trio (MnSi, FeSi, CoSi) that exhibits an anomalous decrease in elastic moduli at low temperatures (see Fig. 12) and, at the same time, reveals the presence of topological points and chiral fermions. A possible relation between these specific features of CoSi can be established in the future. However, recent studies of the magnetoresistance in a topological chiral CoSi crystal in magnetic fields up to 16 T reveal no topological effects [82].

5. Conclusion

This review presents the most important results obtained in conventional studies of the thermodynamic, elastic, and electronic properties of selected transition metal silicides MnSi, FeSi, and CoSi. Unfortunately, due to the limited scope of the review and the area of expertise of the authors, it was not possible to include in it a description of the optical, thermoelectric, and other properties of these substances. However, whenever it was possible, the topological features of the materials associated with the broken crystal symmetry of the substance were stressed.

Acknowledgments. The authors are deeply grateful to I A Abrikosov and M P Belov, who helped to deal with Evaz Isaev's body of work. V Yu Irkhin and S V Streltsov read the manuscript and made a number of helpful remarks, accepted with gratitude by the authors.

This study was supported in part by the Russian Science Foundation (grant no. 17-12-01050P).

References

1. Armitage N P, Mele E J, Vishwanath A *Rev. Mod. Phys.* **90** 015001 (2018)
2. Vanderbilt D *Berry Phases in Electronic Structure Theory: Electric Polarization, Orbital Magnetization and Topological Insulators* (Cambridge: Cambridge Univ. Press, 2018) https://doi.org/10.1017/9781316662205
3. Williams H J et al. *J. Appl. Phys.* **37** 1256 (1966)
4. Dzyaloshinsky I *J. Phys. Chem. Solids* **4** 241 (1958)
5. Moriya T *Phys. Rev.* **120** 91 (1960)
6. Ishikawa Y et al. *Solid State Commun.* **19** 525 (1976)
7. Stishov S M, Petrova A E *Phys. Usp.* **54** 1117 (2011); *Usp. Fiz. Nauk* **181** 1157 (2011)
8. Stishov S M, Petrova A E *Phys. Usp.* **60** 1268 (2017); *Usp. Fiz. Nauk* **187** 1365 (2017)
9. Brando M et al. *Rev. Mod. Phys.* **88** 025006 (2016)
10. Belemuk A M, Stishov S M *Phys. Rev. B* **95** 224433 (2017)
11. Belemuk A M, Stishov S M *J. Exp. Theor. Phys.* **131** 752 (2020); *Zh. Eksp. Teor. Fiz.* **158** 866 (2020)
12. Jaccarino V et al. *Phys. Rev.* **160** 476 (1967)
13. Schlesinger Z et al. *Phys. Rev. Lett.* **71** 1748 (1993)
14. Mandrus D et al. *Phys. Rev. B* **51** 4763 (1995)
15. Paschen S et al. *Phys. Rev. B* **56** 12916 (1997)
16. Fäth M et al. *Phys. Rev. B* **58** 15483 (1998)
17. Mazurenko V V et al. *Phys. Rev. B* **81** 125131 (2010)
18. Ishizaka K et al. *Phys. Rev. B* **72** 233202 (2005)
19. Arita M et al. *Phys. Rev. B* **77** 205117 (2008)
20. Klein M et al. *Phys. Rev. Lett.* **101** 046406 (2008)
21. Ponosov Yu S et al. *JETP Lett.* **103** 316 (2016); *Pis'ma Zh. Eksp. Teor. Fiz.* **103** 359 (2016)
22. Tajima K et al. *Phys. Rev. B* **38** 6954 (1988)
23. Lue C S et al. *Phys. Rev. B* **69** 12511 (2004)
24. Asanabe S, Shinoda D, Sasaki Y *Phys. Rev.* **134** A774 (1964)
25. Sakai A et al. *J. Phys. Soc. Jpn.* **76** 093601 (2007)
26. Nakanishi O, Yanase A, Hasegawa A *J. Magn. Magn. Mater.* **15–18** 879 (1980)
27. Mattheiss L F, Hamann D R *Phys. Rev. B* **47** 13114 (1993)
28. Imai Y et al. *Intermetallics* **9** 261 (2001)
29. Jeong T, Pickett W E *Phys. Rev. B* **70** 075114 (2004)
30. Delaire O et al. *Proc. Natl. Acad. Sci. USA* **108** 4725 (2011)
31. Stishov S M et al. *Phys. Rev. B* **76** 052405 (2007)
32. Stishov S M et al. *J. Phys. Condens. Matter* **20** 235222 (2008)
33. Petrova A E et al. *Phys. Rev. B* **82** 155124 (2010)
34. Petrova A E, Stishov S M *Phys. Rev. B* **86** 174407 (2012)
35. Stishov S M et al. *Phys. Rev. Lett.* **105** 236403 (2010)
36. Lamago D et al. *Phys. Rev. B* **82** 144307 (2010)
37. Alekseev P A et al. *J. Phys. Condens. Matter* **273** 012129 (2011)
38. Stishov S M et al. *Phys. Rev. B* **86** 064433 (2012)
39. Petrova A E, Stishov S M *Phys. Rev. B* **91** 214402 (2015)
40. Petrova A E, Stishov S M *Phys. Rev. B* **94** 020410 (2016)
41. Stishov S M, Petrova A E *Phys. Rev. B* **94** 140406 (2016)
42. Lebech B, Bernhard J, Freltoft T *J. Phys. Condens. Matter* **1** 6105 (1989)
43. Jørgensen J-E, Rasmussen S E *Powder Diffraction* **6** (4) 194 (1991)
44. Sales B C et al. *Phys. Rev. B* **50** 8207 (1994)
45. Wong-Ng W et al. *Powder Diffraction* **2** 257 (1987)
46. Boren B *Arkiv Kemi Mineralogi Geologi A* **11** (1) 1 (1933)
47. Harrison W A *Elementary Electronic Structure* (Singapore: World Scientific, 1999)
48. Ou-Yang T Y, Shu G J, Fuh H R *Europhys. Lett.* **120** 17002 (2017)
49. Nii Y et al. *Phys. Rev. B* **104** L081101 (2021)
50. Baroni S, Giannozzi P, Isaev E *Rev. Mineralogy Geochem.* **71** (1) 39 (2010)
51. Zinoveva G P, Andreeva L P, Geld P V *Phys. Status Solidi A* **23** 711 (1974)
52. Bauer A, Garst M, Pfleiderer C *Phys. Rev. Lett.* **110** 177207 (2013)
53. Fang Y et al. *Proc. Natl. Acad. Sci. USA* **115** 8558 (2018)
54. Vočadlo L et al. *Phys. Chem. Min.* **29** 132 (2002)
55. Marklund K et al. *Phys. Scr.* **9** 47 (1974)
56. Krannich S et al. *Nat. Commun.* **6** 8961 (2015)
57. Zhang T et al. *Phys. Rev. Lett.* **120** 016401 (2018)
58. Miao H et al. *Phys. Rev. Lett.* **121** 035302 (2018)
59. Petrova A E, Stishov S M *J. Phys. Condens. Matter* **21** 196001 (2009)
60. Sarrao J L et al. *Physica B* **199–200** 478 (1994)
61. Nii Y et al. *Phys. Rev. Lett.* **113** 267203 (2014)
62. Luo Y et al. *Phys. Rev. B* **97** 104423 (2018)
63. Mühlbauer S et al. *Science* **323** 915 (2009)
64. Nagaosa N, Tokura Y *Nat. Nanotechnol.* **8** 899 (2013)
65. Adams T et al. *Phys. Rev. Lett.* **121** 187205 (2018)
66. Pshenay-Severin D A, Burkov A T *Materials* **12** 2710 (2019)
67. Dutta P, Pandey S K *Computational Condens. Matter* **16** e00325 (2018)
68. Mooij J H *Phys. Status Solidi A* **17** 521 (1973)
69. Wiesmann H et al. *Phys. Rev. Lett.* **38** 782 (1977)
70. Allen P B, in *Physics of Transition Metals, 1980* (Inst. Phys. Conf. Ser., No. 55, Ed. P Rhodes) (Bristol: The Institute of Physics, 1981) p. 425
71. Lee P A, Ramakrishnan T V *Rev. Mod. Phys.* **57** 287 (1985)
72. Tang P, Zhou Q, Zhang S-C *Phys. Rev. Lett.* **119** 206402 (2017)
73. Pshenay-Severin D A et al. *J. Phys. Condens. Matter* **30** 135501 (2018)
74. Rao Z et al. *Nature* **567** 496 (2019)
75. Xu X et al. *Phys. Rev. B* **100** 045104 (2019)
76. Habe T *Phys. Rev. B* **100** 245131 (2019)
77. Takane D et al. *Phys. Rev. Lett.* **122** 076402 (2019)
78. Wu D S et al. *Chinese Phys. Lett.* **36** 077102 (2019)
79. Wang H et al. *Phys. Rev. B* **102** 115129 (2020)
80. Ni Z et al. *Nat. Commun.* **12** 154 (2021)
81. Seo K et al. *Nano Lett.* **7** 1240 (2007)
82. Petrova A E, Sobolevskiy O A, Stishov S M *Phys. Rev. B* **107** 085136 (2023)